RESEARCH ARTICLE

Key Points:
- Vertical plasma lifting leads to density increase during plume generation phase
- Large downward field-aligned ion flow/flux seen during plume decay phase
- Complex-induced plasma drifts seen indicating plumes' highly dynamic nature

Supporting Information:
- Readme
- Figure S1
- Figure S2
- Movie S1
- Movie S2
- Movie S3
- Movie S4
- Movie S5
- Movie S6
- Movie S7
- Movie S8
- Movie S9
- Movie S10
- Movie S11
- Movie S12

Correspondence to:
S. Zou,
shashaz@umich.edu

On the generation/decay of the storm-enhanced density plumes: Role of the convection flow and field-aligned ion flow

Shasha Zou[1], Mark B. Moldwin[1], Aaron J. Ridley[1], Michael J. Nicolls[2], Anthea J. Coster[3], Evan G. Thomas[4], and J. Michael Ruohoniemi[4]

[1]Department of Atmospheric, Oceanic and Space Sciences, University of Michigan, Ann Arbor, Michigan, USA, [2]Center for Geospace Studies, SRI International, Menlo Park, California, USA, [3]Haystack Observatory, Massachusetts Institute of Technology, Westford, Massachusetts, USA, [4]Department of Electrical and Computer Engineering, Virginia Polytechnic Institute and State University, Blacksburg, Virginia, USA

Abstract Storm-enhanced density (SED) plumes are prominent ionospheric electron density increases at the dayside middle and high latitudes. The generation and decay mechanisms of the plumes are still not clear. We present observations of SED plumes during six storms between 2010 and 2013 and comprehensively analyze the associated ionospheric parameters within the plumes, including vertical ion flow, field-aligned ion flow and flux, plasma temperature, and field-aligned currents, obtained from multiple instruments, including GPS total electron content (TEC), Poker Flat Incoherent Scatter Radar (PFISR), Super Dual Auroral Radar Network, and Active Magnetosphere and Planetary Electrodynamics Response Experiment. The TEC increase within the SED plumes at the PFISR site can be 1.4–5.5 times their quiet time value. The plumes are usually associated with northwestward $\mathbf{E} \times \mathbf{B}$ flows ranging from a couple of hundred m s^{-1} to > 1 km s^{-1}. Upward vertical flows due to the projection of these $\mathbf{E} \times \mathbf{B}$ drifts are mainly responsible for lifting the plasma in sunlit regions to higher altitude and thus leading to plume density enhancement. The upward vertical flows near the poleward part of the plumes are more persistent, while those near the equatorward part are more patchy. In addition, the plumes can be collocated with either upward or downward field-aligned currents (FACs) but are usually observed equatorward of the peak of the Region 1 upward FAC, suggesting that the northwestward flows collocated with plumes can be either subauroral or auroral flows. Furthermore, during the decay phase of the plume, large downward ion flows, as large as ~200 m s^{-1}, and downward fluxes, as large as 10^{14} m^{-2} s^{-1}, are often observed within the plumes. In our study of six storms, enhanced ambipolar diffusion due to an elevated pressure gradient is able to explain two of the four large downward flow/flux cases, but this mechanism is not sufficient for the other two cases where the flows are of larger magnitude. For the latter two cases, enhanced poleward thermospheric wind is suggested to be another mechanism for pushing the plasma downward along the field line. These downward flows should be an important mechanism for the decay of the SED plumes.

1. Introduction

During enhanced geomagnetic activity periods, in particular storms, significant electron density enhancements are often observed in the midlatitude and subauroral region, which are named storm-enhanced densities (SEDs) [*Foster*, 1993]. Often, SEDs extend northwestward to higher latitudes and form a plume. This plume can occasionally be entrained into the cusp region and then enter the polar cap, where it is termed the tongue-of-ionization (TOI) or, if it is not continuous, a polar cap patch, depending on the shape and spatial coverage of the high-density region there [e.g., *Foster et al.*, 2005; *Moen et al.*, 2013]. The SED plume is suggested to be the ionospheric projection of a plasmaspheric plume in the magnetospheric equatorial plane [*Foster et al.*, 2002]. Within the magnetosphere, plasmaspheric plumes can play a crucial role in regulating the dayside reconnection at the magnetopause [*Borovsky et al.*, 2008; *Walsh et al.*, 2014].

Observations using ground-based incoherent scatter radar have revealed elevated F region electron densities, increased ionospheric F_2 layer peak density height (h_mF_2), low electron temperature (T_e), and large convection flows associated with SEDs [*Foster et al.*, 2005, 2007; *Huang et al.*, 2005; *Zou et al.*, 2013]. The low-density midlatitude trough is usually poleward of the SED and eastward of the plume, which results in large density and total electron content (TEC) gradients there. *Zou et al.* [2013] reported >35 TECU per degree of magnetic

latitude (MLAT) during the 24–25 October 2011 intense geomagnetic storm, and the TEC gradient reached 60 total electron content unit (TECU; 1 TECU = 10^{16} el m^{-2}) per degree during the 30 October 2003 superstorm [*Foster and Rideout*, 2005]. Such large TEC gradients may have a profound impact on radio communication and navigation systems [*Ledvina et al.*, 2002; *Doherty et al.*, 2004; *Skone et al.*, 2004; *Coster and Skone*, 2009; *Sun et al.*, 2013] and therefore motivate continued study of the SED/trough evolution and generation mechanisms.

An electron density increase observed by an instrument fixed on the Earth's surface can be due to one or more of the following three general mechanisms: transport (zonal or latitudinal), enhanced local production, and reduced loss with continued production. In addition, at different latitudinal locations, the dominant mechanism for the density enhancement may also be different.

Foster [1993] suggested that the SED plume is produced as the high-latitude convection electric field moves equatorward and picks up high-density plasma from lower latitudes and transports them toward the cusp. Observations from the Chatanika radar [*Foster and Doupnik*, 1984; *Foster*, 1993] and Super Dual Auroral Radar Network (SuperDARN) [*Thomas et al.*, 2013] support this scenario. The remaining outstanding questions are as follows: what is the nature of the electric field, where does it map to in the magnetosphere, and whether there is any additional mechanism working within the plumes to increase the density.

Besides zonal transport, transport across a large range of latitudinal regions is suggested to account for the seed population density increase. A superfountain effect has been invoked to explain the SED formation during superstorms when the *Dst* index drops to lower than −250 nT [*Tsurutani et al.*, 2004; *Mannucci et al.*, 2005], and as a result, the peak of the low-latitude ionization anomaly can be pushed from the nominal ~±10° to ~±25° to 40° magnetic latitudes [*Tsurutani et al.*, 2013; *Lu et al.*, 2013]. For geomagnetic storms with lower intensity, the superfountain effect is not believed to be able to account for the density increase at higher latitudes [*Huang et al.*, 2005; *Zou et al.*, 2013]. *Huang et al.* [2005] reported a 2–4 times *F* region peak density enhancement at ~53° MLAT over Millstone Hill and suggested that penetrating eastward electric fields and the associated northward flows lead to the density increase. In a more recent study, *Zou et al.* [2013] reported observations from multiple instruments, including Poker Flat Incoherent Scatter Radar (PFISR) and SuperDARN, and they also suggested that large vertical flows associated with northwestward convection flows play the dominant role for the density increase over Alaska (>65° MLAT). Equatorward thermospheric wind and particle precipitation also contribute but to a lesser degree. In both cases mentioned above, the minimum *Dst* reached about ~ −130–150 nT, so the storms are categorized as intense storms and are of much smaller magnitude than the superstorms.

The effect of such vertical flows has been examined in the global ionosphere-thermosphere model (GITM) and found to be of great importance on the global high-latitude density redistribution [*Deng and Ridley*, 2006]. In addition, using a stand-alone Utah State University Time-Dependent Ionospheric Model (TDIM) [*Heelis et al.*, 2009] and a coupled TDIM and inner magnetosphere model [*David et al.*, 2011], both studies suggested that the SED increase can be due to the northward component of the convection flows in the sunlit region and the density is increased locally due to reduced loss and continued production while the plasma is moved to higher latitudes. *Wang et al.* [2010] conducted a comprehensive model using a global magnetosphere model Lyon-Fedder-Mobarry coupled with the thermosphere-ionosphere electrodynamics general circulation model (TIEGCM) and data comparison for three storms. Two of the storms were intense and one was a superstorm. They found that the penetration electric field is also important for the density increase in the dayside low latitudes and midlatitudes.

Another way to reduce the plasma loss is to mechanically push the plasma to higher altitudes taking advantage of ion-neutral collisions. The equatorward thermospheric wind can induce such an upward ion drift along the magnetic field line. This mechanism is found to be very important during the storm recovery phase and at midlatitudes [*Lu et al.*, 2012] and contributes to the vertical flows near the poleward edge of the SED base region [*Zou et al.*, 2013].

The convection flows associated with SEDs are suggested to be subauroral polarization streams (SAPS), which are enhanced westward flows with average magnitude of ~400 m s^{-1} and average flow channel width of 3°–5° [*Yeh et al.*, 1991; *Foster and Burke*, 2002; *Foster and Vo*, 2002]. Usually embedded within the SAPS are narrow (~1°) subauroral ion drifts [*Spiro et al.*, 1979] or polarization jets [*Galperin et al.*, 1974] with flow magnitude higher than 500 m s^{-1} [*Spiro et al.*, 1979] or 1 km s^{-1} [*Anderson et al.*, 1991]. The selection of the velocity threshold seems arbitrary.

The SAPS flows are suggested to be due to the downward Region 2 field-aligned currents (FACs) closing in a low-conductance region [*Southwood and Wolf*, 1978]. However, since SEDs are associated with density enhancement in sunlight while the SAPS are expected to occur in a low-density region, *Fuller-Rowell* [2011] commented that these two explanations seem to contradict each other. Indeed, *Whalen* [1989] observed sunward transport of low density to the dayside-forming dayside trough. In a more recent study, *Zou et al.* [2013] also reported a longitudinally extended trough intruding to the dayside region due to the SAPS in the duskside convection cell.

In order to find the nature of the convection flows that are collocated with these enhanced or reduced plasma density in the SED and dayside trough regions, knowledge about the associated FAC distribution as well as the plasma temperature within these regions is required, because the large-scale FAC distribution, i.e., Region 1 and Region 2 FAC systems, provides a way of morphologically mapping phenomena between the magnetosphere and the ionosphere. It is now possible to regularly have such simultaneous observations because of the global coverage of Active Magnetosphere and Planetary Electrodynamics Response Experiment (AMPERE) [*Anderson et al.*, 2000, 2002].

Foster [1993] mentioned a downward plasma velocity component along the magnetic field line in the SED base region at midlatitude. However, to the best of our knowledge, the direction and magnitude of the field-aligned flow and ion flux within the plume region have not been reported before. Besides recombination, such field-aligned plasma motion is another factor that could affect the density profile of a plume and thus its lifetime. Therefore, it is also one of our goals to investigate the field-aligned flow and ion flux in the SED plumes.

2. Instrumentation

2.1. GPS TEC

One of the most utilized parameters to quantify the ionospheric electron density is the TEC, which can be calculated using the different group and phase delays of the two transmitted frequencies from dual frequency Global Navigation Satellite System, including Global Positioning Satellite (GPS). Recent years have witnessed an increased interest in investigating the ionospheric density variations, such as SEDs and TOIs, during geomagnetic disturbances due to the fast-growing number of ground-based GPS receivers and the resulting regional- or even global-scale 2-D GPS TEC maps [*Mannucci et al.*, 1998; *Saito et al.*, 1998; *Rideout and Coster*, 2006]. The GPS vertical TEC data in this study are obtained from the Madrigal database. The processed and binned TEC data have spatial resolution of $1° \times 1°$ in geographical coordinates and temporal resolution of 5 min. Detailed information about the data processing procedure has been described in *Rideout and Coster* [2006]. The data have been converted to Altitude Adjusted Corrected Geomagnetic (AACGM) coordinates for this study.
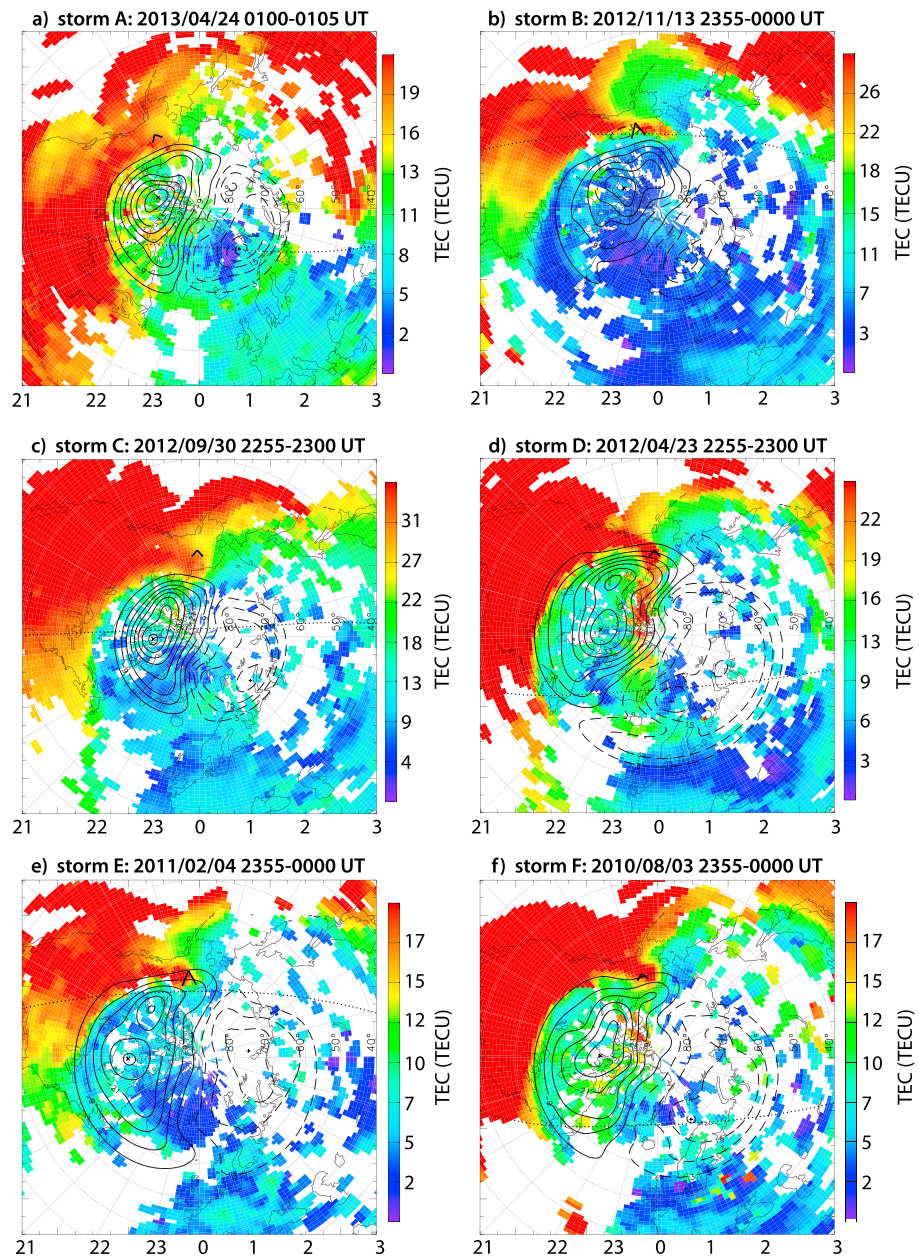
2.2. SuperDARN

The Super Dual Auroral Radar Network (SuperDARN) is an international collaboration operating high-frequency coherent radars in both the Northern and Southern Hemispheres [*Greenwald et al.*, 1995; *Chisham et al.*, 2007]. They enable imaging the large-scale ionospheric convection and thus electric fields with high temporal resolution (about 1 or 2 min). The newly deployed midlatitude radars extend the field of view of the existing SuperDARN radars to latitudes as low as 50° and provide better ionospheric convection measurements during strong driving periods, such as geomagnetic storms.

2.3. PFISR

PFISR is one face of the Advanced Modular Incoherent Scatter Radar facilities that have been used to conduct studies of the upper atmosphere and to observe space weather events. The electronic steering capability enables nearly simultaneous measurements in multiple directions. Besides the density and convection flows, it also provides a plasma temperature measurement and the field-aligned flow through beam pointing along the magnetic field line.

2.4. AMPERE

The global-scale FACs distribution is made available because of the Active Magnetosphere and Planetary Electrodynamics Response Experiment (AMPERE). Magnetic perturbations measured by the Iridium satellites have been processed using spherical harmonic procedures [*Anderson et al.*, 2000, 2002] to obtain the FACs distribution at 1 h magnetic local time (MLT) and 1° magnetic latitude resolutions from 40° to 90° MLAT in AACGM coordinates.

Figure 1. Selected 2-D GPS VTEC observations of the SED plumes during six geomagnetic storms. Ionospheric equipotential contours derived from the SuperDARN radar observations are superposed as solid and dashed black lines. PFISR field of view is outlined by black segments and the terminator is also shown as a dotted line in each frame.

3. Multiple-Event Observations

Figure 1 shows selected 2-D GPS vertical TEC (VTEC) observations of plumes during six geomagnetic storms. The storms are listed in Table 1. Ionospheric equipotential contours derived from the SuperDARN radar observations in the corotating reference frame are also superposed [*Ruohoniemi and Baker*, 1998; *Shepherd and Ruohoniemi*, 2000]. In each frame, magnetic noon/midnight is at the top/bottom, and dusk/dawn is toward the left/right. The selection criteria are (1) a clear plume signature over Alaska and (2) that PFISR observed at least part of the plume. Events are organized from the most recent storm to earlier storms. Because of the mismatch between the geomagnetic and geographic poles, SED plumes occur frequently over Alaska and western Canada. In addition, because of the dense GPS receivers distributed within this area, the data coverage is very good. The terminator is also shown as a dotted line in each frame. As can be seen, the plumes always

Table 1. A List of All Six Storm Events, Quiet Days of Which the TEC Measurements Are Used for Comparison in Figure 2, Minimum SYM-H for the Storm, Maximum TEC Measured at PFISR, the Ratio Between the Storm Time TEC Peak and the Quiet Time TEC at the Same Time as the Observed TEC Peak, and Geometries of Induced Plasma Flows Inferred From PFISR Observations[a]

| Storm Labels	Storm Dates (Day of the Year)	Quiet Days (Day of the Year)	Min (*SYM-H*)	Max TEC at PFISR	Ratio (TECs/TECq) at UT(Max TECs)	Geometries of Induced Plasma Flows Observed Within Plumes[a]
A	23–24 Apr 2013 (113–114)	22–23 Apr 2013 (112–113)	−52	21.60	1.62	b
B	13–14 Nov 2012 (318–319)	9–10 Nov 2012 (314–315)	−118	24.33	1.89	lower latitude: a, c; higher latitude: a
C	30 Sep to 1 Oct 2012 (274–275)	28–29 Sep 2012 (272–273)	−138	36.73	1.36	a, b, and c
D	23–24 Apr 2012 (114–115)	29–30 Apr 2012 (120–121)	−125	30.63	2.17	a and b
E	4–5 Feb 2011 (35–36)	3–4 Feb 2011 (36–37)	−67	17.66	2.70	lower latitude: a, c, and d; higher latitude: a, b
F	3–4 Aug 2010 (215–216)	21–22 Aug. 2010 (232–233)	−81	21.35	5.47	a, d

[a]The four geometries of induced plasma flows are shown in Figure 10.

form in the sunlit region. Movies of 2-D GPS VTEC polar views for all six storms are provided as supporting information. Among these six events, the April 2012 storm (storm D) is featured with an obvious elongated tongue of ionization across the polar cap connected to the plume. The plasmas supplied by the SED plume were transported by the antisunward convection flows in the polar cap toward the nightside.

The solar wind dynamic pressure and interplanetary magnetic field (IMF) B_y (blue) and B_z (red) components in GSM coordinates for all six events are shown in Figure 2. Also plotted are the *SYM-H* index, representing the ring current strength, and the VTEC value observed at the PFISR site (red). The black curve in Figures 2a–2f shows the quiet time TEC values for comparison. The quiet days are selected based on the monthly geomagnetic indices bulletins published by National Oceanic and Atmospheric Administration. Movies of 2-D GPS VTEC polar views for all quiet times are provided as supporting information. Five out of the six plumes are observed at the PFISR site during the main phase of the storms. Only during the February 2011 storm (storm E), the plume was observed during the early recovery phase. As listed in Table 1, the peak plume TEC value observed at PFISR site ranges from 17.66 TECU to 36.73 TECU and the ratio between the peak plume TEC value and the value at the same UT but of quiet days ranges from 1.36 to 5.47. Comparing the storm time and quiet time TEC curves, one can see that on the side of the SED plumes signature, there is often a decrease in TEC, which is a dayside trough. These dayside troughs have been observed by other instruments before, such as ground-based ionosondes [*Whalen*, 1989] and are termed morning and afternoon troughs depending on which convection cell they are located in.
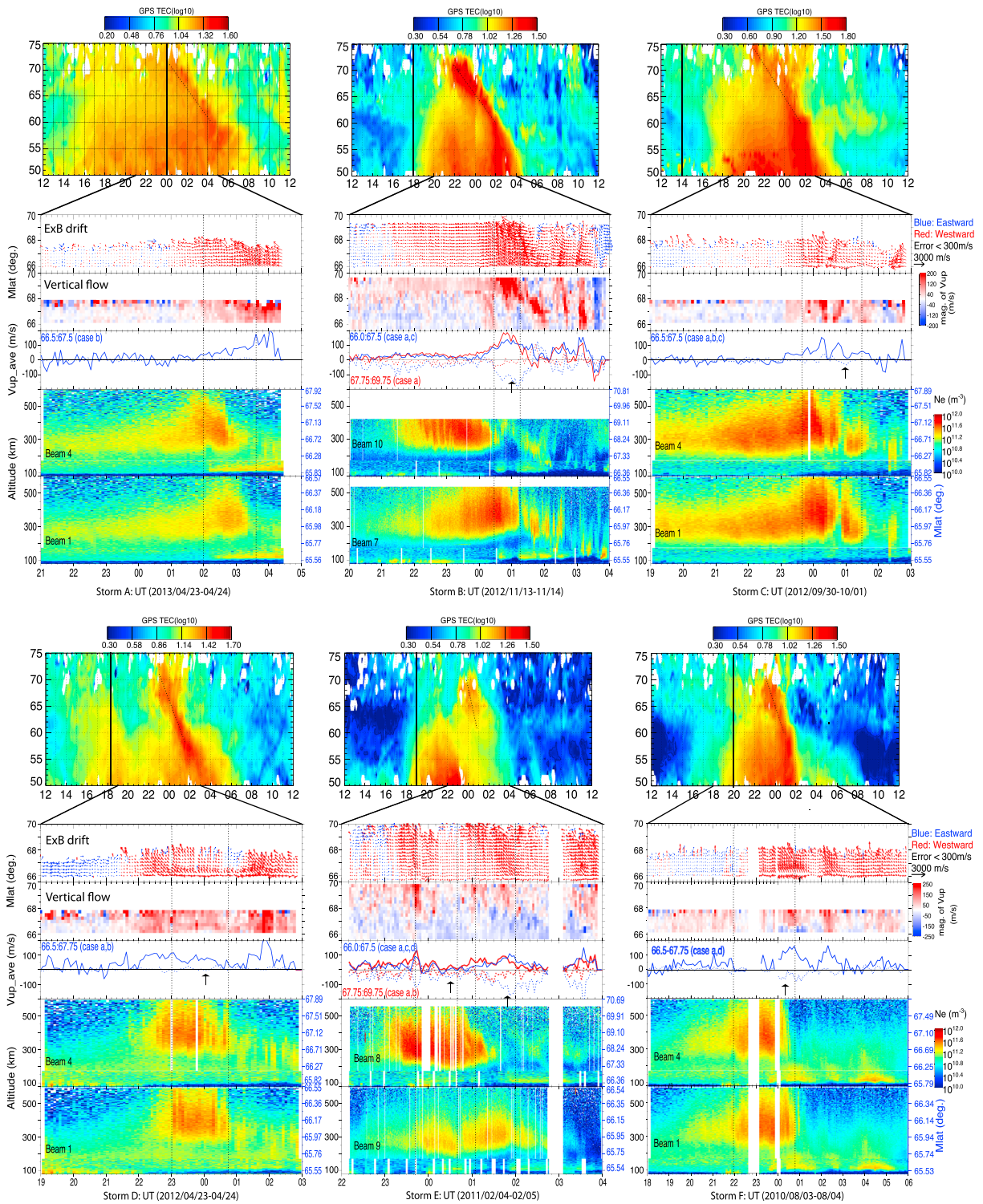
Figure 3 shows PFISR observations of the $\mathbf{E} \times \mathbf{B}$ convection flow (vectors), the vertical flow (V_z) calculated from the convection flow and the antiparallel flow, the latitudinally averaged vertical flow contributed from the convection flow ($V_{z\_E \times B}$, solid) and the antiparallel flow (V_{z_ap}, dotted), respectively. Calculations of the convection and antiparallel flows are based on *Heinselman and Nicolls* [2008]. At PFISR, the vertical component due to $\mathbf{E} \times \mathbf{B}$ drift $V_{E \times B}$ is $V_{E \times B} \cos I$, i.e., ~$0.2 V_{E \times B}$, while that due to the antiparallel flow is V_{z_ap}, i.e., ~$0.98 V_{ap}$. Electron density vertical profiles from two beams (one looking at the highest latitudes and one looking vertically in geographic coordinates) are shown at the bottom. The magnetic latitudes of these two beams are labeled on the *Y* axis on the right. Arrows and two dotted vertical lines are described in the field-aligned ion flux study later in the text, which are associated with Figures 6 and 7.

Also plotted are the time series of GPS VTEC at the longitude of PFISR and from 50° to 75° magnetic latitudes (Figure 3, top), providing a larger-scale context for interpreting the PFISR observations. Time series of TEC at the longitude of PFISR during the corresponding quiet times are also included as supporting information. In each storm event, the beginning of the storm main phase, i.e., the time when *SYM-H* became negative, is marked with a black solid vertical line and the SED plume is highlighted by a black dashed vertical line. In five out of six cases, the SED plumes manifest as high-TEC region extending from lower latitudes to higher latitudes, lending support to the transport of a seed population due to horizontal flows. The only exception is the event in February 2011 (storm E), during which the plume was an isolated high-TEC region. The reason is that the plume was observed during the early recovery phase, and the high-TEC region at lower latitudes already entered into the negative storm phase. This is evident in the movie.
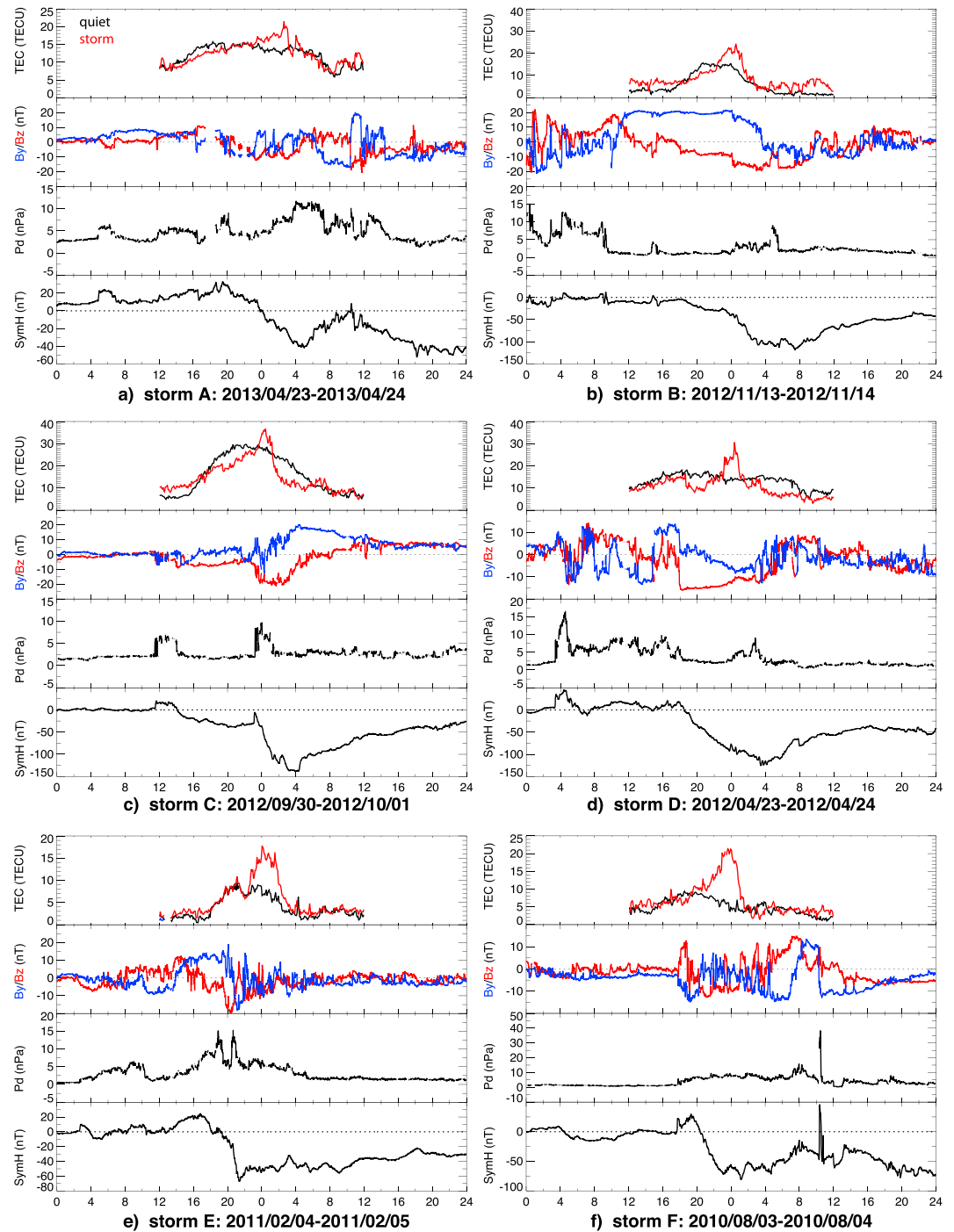
Figure 2. (a–f) IMF B_y (blue) and B_z (red) components in GSM coordinates, the solar wind dynamic pressure, and the *SYM-H* index are shown for all six events. (top) The GPS TEC value observed at the PFISR site during this time period, shown as a red line, while the black line shows the quiet time TEC value for comparison.

During the two storms on November 2012 (storm B) and February 2011 (storm E), PFISR was operating in an 11-beam, high-duty-cycle mode and the latitudinal coverage was larger than the other four cases, when it was operating in the low-duty-cycle four-beam international polar year mode [*Sojka et al.*, 2009]. Therefore, for these two storms, the upward flows within the radar field of view (FOV) are grouped into two latitudinal ranges and then averaged. In other cases, the upward flows are averaged over the whole radar FOV.

Figure 3. PFISR observations of the **E** × **B** convection flow (vectors), the equivalent vertical flow (V_z) calculated from the convection flow and the antiparallel flow, the latitudinally averaged vertical flow contributed from the convection flow ($V_{z\_E\times B}$, solid) and the antiparallel flow (V_{z_ap}, dotted), respectively. (bottom) Electron altitude profiles measured by two beams (one with lowest elevation angle and one vertical beam). (top) Time series of GPS TEC at the longitude of PFISR and from 50° to 75° magnetic latitudes, providing a larger scale context for understanding the PFISR observations. Time series of TEC at the longitude of PFISR during the corresponding quiet times are included as supporting information.
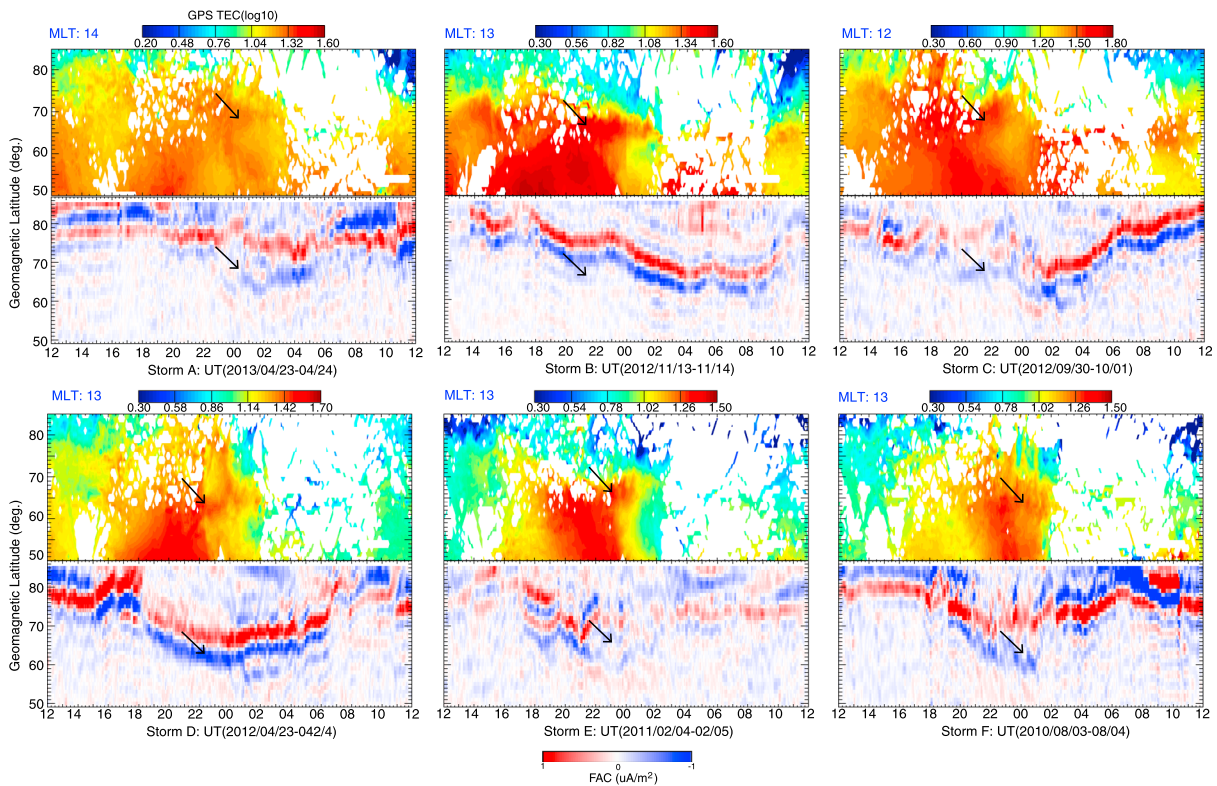
Figure 4. Time series of GPS TEC and AMPERE FACs at a fixed postnoon MLT are shown for all six events. Time series of TEC at the same fixed postnoon MLT during the corresponding quiet times are included as supporting information.

In all cases, high-density plumes are associated with northwestward convection flows and also vertical flows, the magnitude of which range from a couple of tens $m\,s^{-1}$ to over a hundred $m\,s^{-1}$. Comparing the solid and dotted curve in the fourth row, the antiparallel flow contribution is, in general, negative or close to zero and, therefore, the upward flow is mainly due to the $\mathbf{E} \times \mathbf{B}$ convection flow projection in the vertical direction. During the November 2012 (storm B) and February 2011 storms (storm E), when PFISR had the wider latitudinal coverage, the upward flows at the higher-latitude group were larger and more persistent than that at the lower latitude group. This vertical flow calculation is consistent with the density observation shown in the bottom two panels. That is, the density enhancement at higher latitudes is observed at earlier times and usually of larger magnitude.

The verticals flows at the lower latitude group were frequently negative with intermittent positive values. These intermittent flow changes are likely due to penetration electric fields. Such an example can be seen between 00 UT and 01 UT in the 13 and 14 November 2012 event (storm B). There is a further southward turning in the IMF B_z at ~00 UT in Figure 2b, and the $\mathbf{E} \times \mathbf{B}$ drift increased at nearly the same time. Upward flows due to this penetration electric field are apparent between 0000 and 0030 UT. After 0030 UT, the upward flows decayed due to large downward field-aligned flows. Such downward flows are described and discussed further later in the text. The density enhancement measured by the vertical beam due to this sudden penetration electric field is evident in Figure 3 (storm B, bottom).

For all six cases, the largest convection flows and the largest upward flows are observed in the low-density trough region east of the plumes, i.e., after the observation of the plume. The relation between the flow, density, and FACs are further discussed in section 4.

In order to study the FAC distribution within the plume, time series of GPS TEC and FACs from AMPERE at a fixed postnoon MLT are plotted in Figure 4. This format is chosen because the plume, once formed, tends to be stable or moves slowly across different MLTs. This presentation also allows an examination of the temporal evolution of the FACs. In addition, the AMPERE data are provided at 1 h of MLT spatial resolution. The big data gap in each panel is due to lack of receivers over the Pacific Ocean. Time series of TEC at the same fixed postnoon MLT during the corresponding quiet times are also included as supporting information. In five out of six cases, a pair of
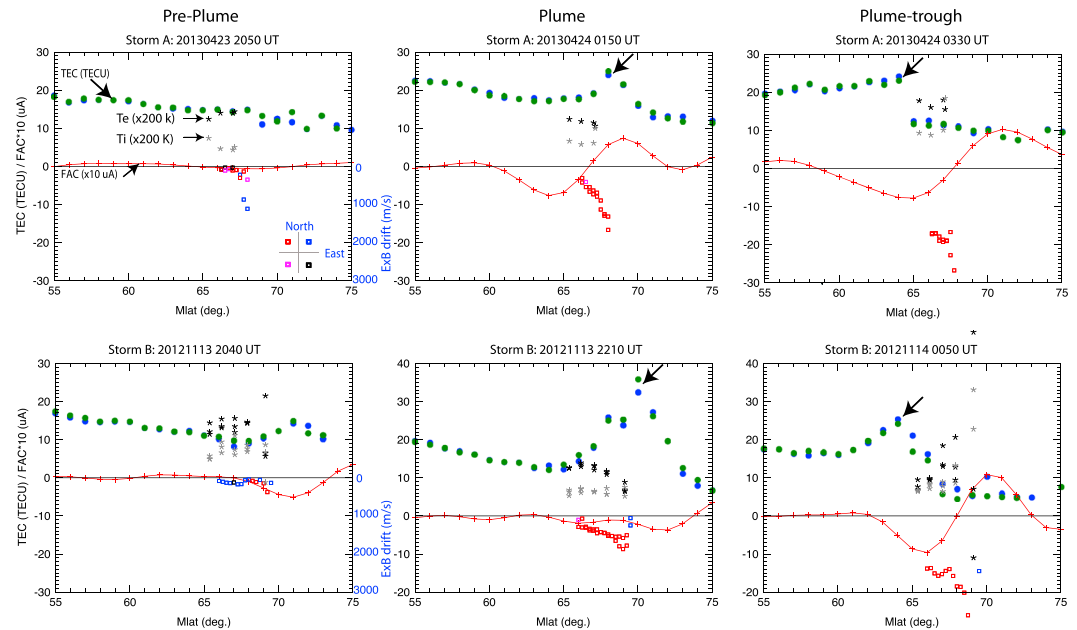
Figure 5. In each panel, FACs (red line), plasma temperature at 400 km (asterisks, black for T_e and grey for T_i) and convection flows (squares) are plotted. The color of the convection flows represents the flow direction: red for northwestward, blue for northeastward, magenta for southwestward, and black for southeastward. Each row represents one storm event, and the three columns indicate the preplume, within plume and plume-trough conditions. Black arrows in the middle and right columns highlight the plumes.

enhanced FACs with upward at higher latitudes and downward at lower latitudes is evident, and they are moving gradually equatorward. The polarity of the FAC pair is the same as the Region 1 and Region 2 pair on the dayside. The equatorward motion is consistent with the *SYM-H* index evolution shown in Figure 2. That is, during the storm main phase, the polar cap area is expanding and the FAC systems are moving equatorward. The FACs during the February 2011 storm (storm E) became weaker but still stayed at roughly the same latitudes. This is because this storm just entered into the recovery phase. The plume signatures and their corresponding FACs are highlighted by arrows. One can see that the plumes are generally associated with the downward Region 2 FACs and the equatorward part of the upward Region 1 FACs.

The AMPERE FACs and the GPS TEC provide large-scale context for understanding the PFISR data, while PFISR data provide detailed ionospheric parameters within the plume. In Figure 5, FACs (red line), plasma temperature at 400 km (asterisks, black for T_e and grey for T_i), convection flow magnitudes (squares) are plotted in each panel. As for the convection flows, the color represents the flow direction: red for northwestward, blue for northeastward, magenta for southwestward, and black for southeastward. Two representative storm events, i.e., April 2013 (storm A) and November 2012 (storm B) storms, are selected to show in two rows, and the three columns indicate the preplume, plume, and plume-trough conditions. Several important observations can be seen here.

Within the plumes, the convection flows are usually westward, but the magnitude of the flows ranges from a couple of hundred m s^{-1} to more than 1 km s^{-1}. The FACs within the plumes can also be upward or downward. However, in five out of six cases, the plumes are equatorward of the upward Region 1 FAC peak. The only exception is the April 2012 storm (storm D) event, which is also the only TOI event in our list. During this event, the plume and the TOI that extended into the polar cap cannot be separated easily because the location of the open-closed field line boundary is not known for sure. It is very likely that the upward FAC and the flow shear are signatures of the cusp. However, the spatial resolution of the AMPERE data and the possible artificial FACs due to the spherical harmonic procedure prevented further detailed comparison of the plumes and the FAC distribution.

Before the plume forms, the ion temperature at 400 km is usually several hundred K and the electron temperature roughly double this. Within the plumes, the electron temperature clearly decreases and becomes comparable to the ion temperature, while the ion temperature is not affected. At the transition region between the plume and the trough, both ion and electron temperatures start to increase. Without an
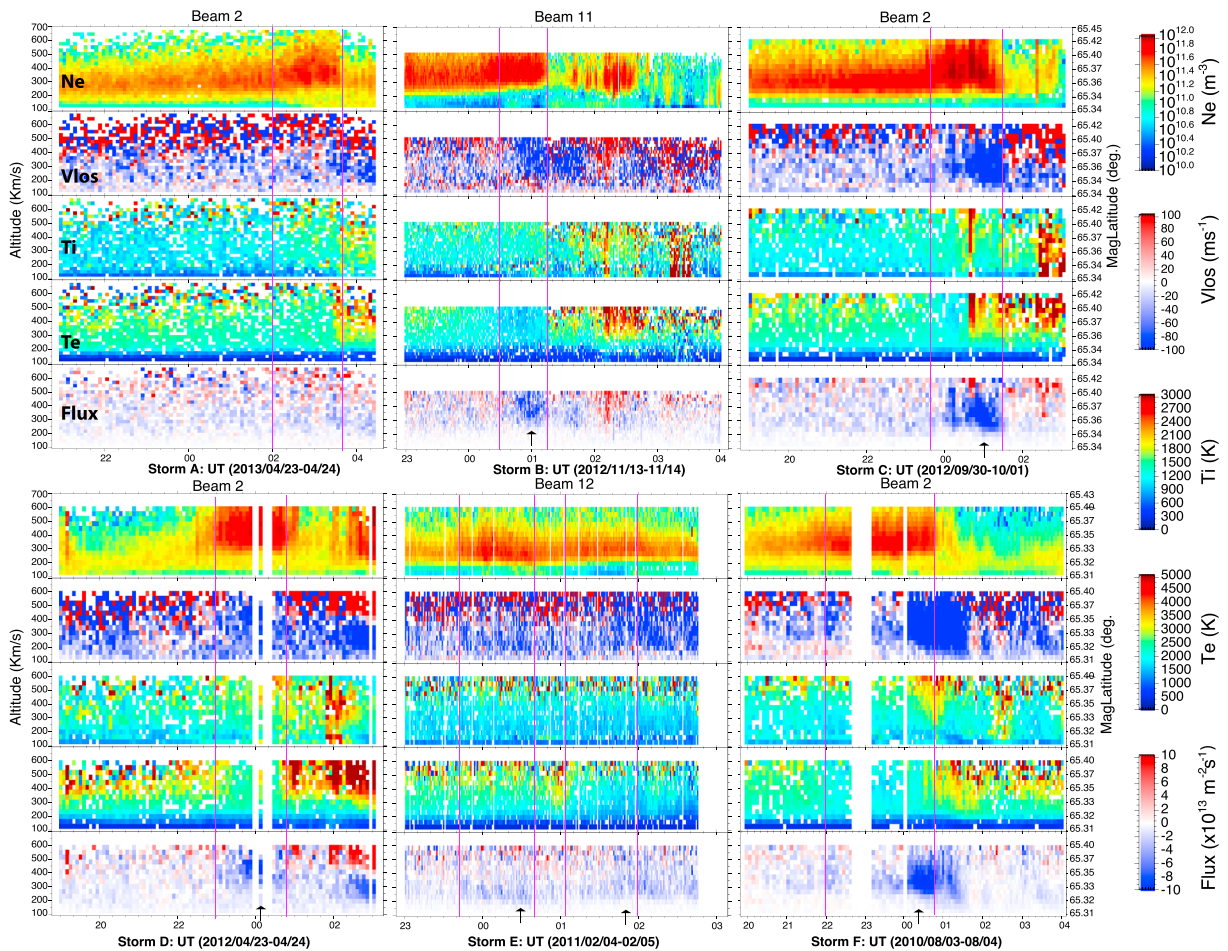
Figure 6. PFISR up-B beam measurement of the electron density, antiparallel ion velocity, ion and electron temperatures, and the calculated ion flux assuming charge neutrality.

additional heat source, the electron temperature should be inversely proportional to the number density. This could explain the electron temperature changes within the plume and in the plume-trough transition region. However, in the trough region, the electrons may be heated further by heat transferred from the ring current region. In the plume region, this effect is diluted by the large electron density. On the other hand, the ion temperature increase is also seen simultaneously with large convection flows in the trough, as large as 2.5 km s^{-1}, indicating significant frictional heating. The enhanced ion temperature can lead to rapid loss of plasma due to heat transfer between ions and electrons and thus enhanced recombination rate, as well as enhanced field-aligned flows [Sellek et al., 1991; Pintér et al., 2006].

Figure 6 shows the electron density, antiparallel ion velocity, ion and electron temperatures measured by the PFISR beam pointing along the magnetic field line, and the calculated ion flux assuming charge neutrality. Note that this magnetic field-aligned beam is located at ~65.4° MLAT, the lowest of all PFISR beams. As shown in the bottom panel for each event, large downward field-aligned ion fluxes were often (five out of six events) seen in the SED plumes. This is consistent with the calculated vertical flows at the lowest latitude shown for each event in Figure 3, which are often of negative values. That is, the projection of the field-aligned downward flows in the vertical direction exceeded that of the **E** × **B** drifts and led to net downward vertical flows. Arrows are drawn to highlight the peak downward flux in Figure 6 and vertical projection of the field-aligned flows in Figure 3. During the April 2013 event (storm A), no obvious downward field-aligned flows were observed and the vertical flows in Figure 3 were always positive. During the 30 September 2012 storm (storm C), a diverging field-aligned ion flow event, i.e., upard at higher altitude and downward at lower altitude, also occurred sporadically at ~0040 UT on 1 October and lasted for ~10 min. This diverging ion flow event is associated with intense short time heating in both electrons and ions.
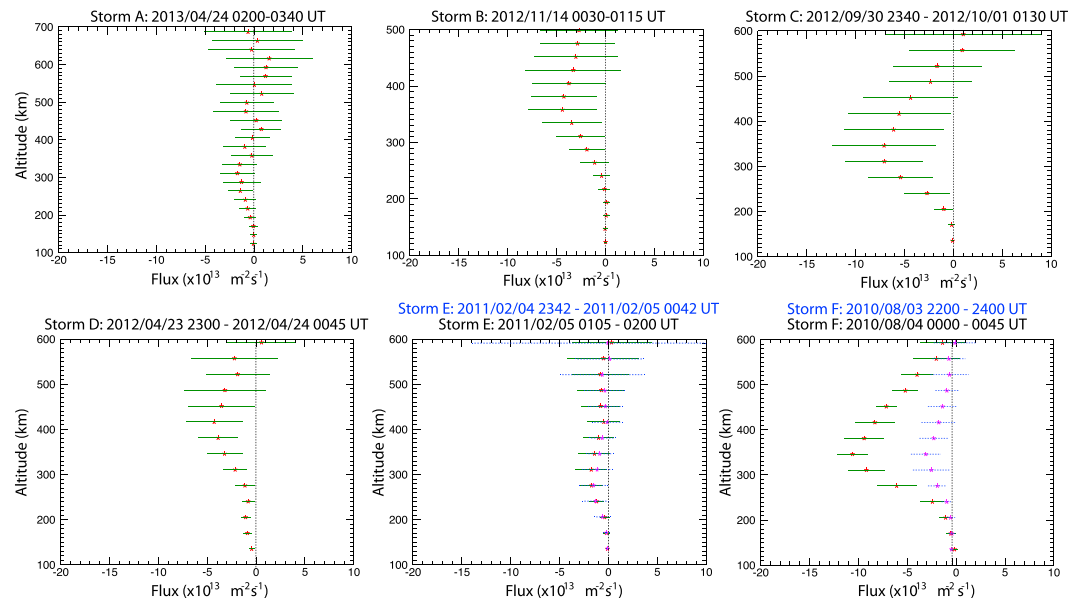
Figure 7. Altitude profiles of averaged ion flux calculated based on PFISR observations. Red asterisks indicate the mean, and green segments indicate the standard deviation. If there are two time periods averaged for one event, the mean and standard derivation associated with the first time period are colored magenta and blue.

To get a quantitative estimate, ion fluxes observed between the times indicated by the two adjacent magenta vertical lines are averaged and plotted in Figure 7. The same periods are also marked in Figure 3. Figure 7 shows the altitude profiles of ion flux averaged over the chosen time periods. PFISR observations within the denoted time slot are averaged and red asterisks indicate the mean, while green segments indicate the standard deviation. If there are two time periods averaged, the mean and standard derivation associated with the first time period are colored magenta and blue, respectively. Four out of six events are associated with substantial ion field-aligned downward flux, and the peak mean downward fluxes ranged from ~4 to ~10×10^{13} m^{-2} s^{-1}. The magnitude of the downward flux is comparable to the sunward flux observed by DMSP satellite in the SED plume reported by *Foster et al.* [2014]. The altitude where the downward flux reached its peak is ~350 km for three cases and ~410 km for one case. Below the flux peak, the gradient of the flux decrease is negative. This is expected because of the rapid dissociative recombination. Above the flux peak, the gradient changes to positive up to ~500 or 600 km, which varies case by case, and this suggests that there should be ionization source within this region. Solar production and/or particle precipitation could be an ionization source. But in regions where reduced electron temperature is observed together with the downward flux, solar production is the most likely dominant source.

4. Discussion

4.1. Convection Flow and FACs Within the SED Plumes

It is found that the equatorward meridional wind plays a significant role for the density increase at midlatitudes [*Lu et al.*, 2012] and also contributes to the density increase near the poleward boundary of the SED base region [*Zou et al.*, 2013]. Within the SED plumes, as shown in Figure 3, the vertical flows ranging from a couple of tens of m s^{-1} to over a hundred m s^{-1} are observed for all cases and are nearly all due to the $\mathbf{E} \times \mathbf{B}$ convection flow projection in the vertical direction. The antiparallel flows are close to zero or negative, suggesting that the meridional wind does not contribute to the density increase in the plumes. This finding contributes to the overall understanding of the thermospheric wind effect for SED.

It is also found that the plumes are associated with northwestward flows and can be collocated with either upward or downward FACs but usually equatorward of the peak of the Region 1 upward FACs. It is expected that downward flowing electrons from the magnetosphere are the main upward field-aligned current carriers, therefore, the equatorward boundary of the upward FACs can be viewed as the equatorward boundary of the electron plasmas sheet or auroral oval. This suggests that the northwestward flows
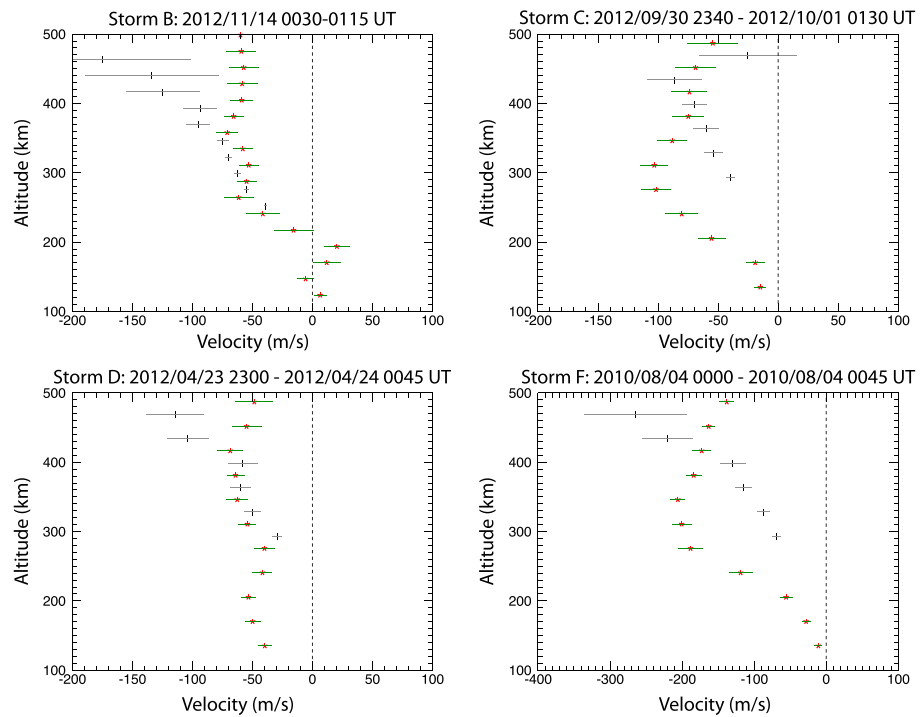
Figure 8. Averaged field-aligned flow speed (red asterisks) measured by PFISR for the four events where apparent enhanced downward flows were observed and the calculated ambipolar diffusion flow speed (black vertical bar).

collocated with plumes can be either subauroral or auroral flows. On the duskside, equatorward of the electron plasma sheet often resides the precipitating protons, which can be a significant ionization source in this region. Evidence of energetic proton precipitation can be seen near the latter half of the plumes in Figure 3 for April 2013 (storm A), November 2012 (storm B), February 2011 (storm E), and August 2010 (storm F) storms, that is, the ionization that is concentrated within a thin layer between 120–150 km. Further calculation of the height-integrated conductance (not shown) using PFISR measurements shows that the ion precipitation contribution to the conductance increase is usually several mho in these events. Therefore, even if the flow is collocated with the downward Region 2 FACs and is thus in the subauroral region, the conductance is not necessarily low because of the ionization due to ion precipitation. In addition, although within the plumes, the topside ionospheric densities increase significantly, calculations show that its contribution to the conductance is minimal.

4.2. Field-Aligned Flows Within the SED Plumes

In section 3, the field-aligned beam frequently observed large downward ion flows within plumes during the decay phase. Opposite to the upward lifting, these downward flows push plasma to a lower altitude where the recombination rate is higher and thus result in enhanced loss. Large field-aligned downward flows on the dayside have been observed by EISCAT during disturbed periods ($Kp > 5$) [*Ogawa et al.*, 2009]. They suggested that the cusp moved equatorward of the radar site, and the radar was measuring the ballistic return of upward flowing ions. The ballistic return of outflowing ions has been observed using the DE 2 satellite [*Loranc et al.*, 1991] and studied using simulations [*Loranc and St.-Maurice*, 1994]. In our cases, five out of six plumes are observed near the equatorward boundary of the convection pattern and electron temperature decrease is observed within the SED; therefore, it is unlikely that plumes extended to or beyond the cusp in these cases and so the ballistic return explanation is not applicable for these cases.

The measured antiparallel flow V_{ap} is the equatorward meridional wind projected along the magnetic field ($U_s \cos I$) minus the ambipolar diffusion (V_d). The significant density increase in the F region and the associated temperature decrease are expected to modify the field-aligned pressure gradient and then the ambipolar diffusion velocity. Therefore, we first calculate the ambipolar diffusion velocity to see whether it would account for the enhanced downward flow. The ambipolar diffusion calculation is done using the
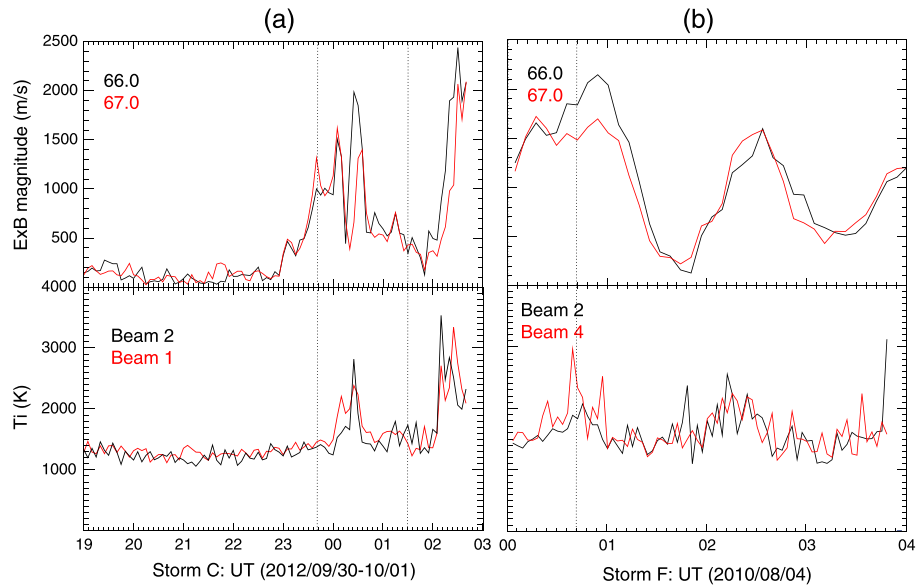
Figure 9. $E \times B$ drift magnitude at 66° and 67° MLATs, and ion temperature averaged between 150 and 600 km from the field-aligned beam (beam 2) and one representative beam at higher latitude are shown for the 30 September to 1 October 2012 (storm C), and 3–4 August 2010 (storm F) storms.

following equation [e.g., *Buonsanto and Witasse*, 1999; *Aponte et al.*, 2005] for altitudes where O^+ concentration is $> 90\%$ of the total ions.

$$V_d = -2D_{in} \frac{T_p}{T_r} \sin I \left(\frac{1}{n_e} \frac{dn_e}{dz} + \frac{1}{T_p} \frac{dT_p}{dz} + \frac{0.36}{T_r} \frac{dT_r}{dz} + \frac{1}{H_p} \right)$$

where I is the magnetic dip angle, D_{in} is the ion-neutral diffusion coefficient, given by $D_{in} = \frac{K_b T_r}{m_i v_{in}}$. $T_p = \frac{(T_i + T_e)}{2}$, $T_r = \frac{(T_i + T_n)}{2}$, and $H_p = \frac{2K_b T_p}{m_i g}$ is the plasma scale height. T_i, T_e, and N_e are observed by PFISR and T_n and the concentration of O, O_2, and N_2 are from the NRL-MSISE-00 model [*Picone et al.*, 2002]. The ion-neutral collisional frequency is the sum of collision frequency between the atomic oxygen with three major atom and molecule species. That is,

$$v_{in} = v_{O^+,O} + v_{O^+,N2} + v_{O^+,O2}$$

Figure 8 shows the averaged field-aligned flow speed measured by PFISR for the four events where apparent enhanced downward flows were observed and also the calculated ambipolar diffusion flow speed. The ambipolar diffusion flow speed was comparable to that of the measured field-aligned flow for the November 2012 (storm B) and April 2012 (storm D) storms, while it can only account for roughly half of the measured downward flows for the September 2012 (storm C) and August 2010 (storm F) storms. The differences between the measured and the calculated flow at the altitude where the downward flow speed reached the peak are $\sim 50 \, \text{m s}^{-1}$ and $\sim 120 \, \text{m s}^{-1}$, respectively. Possible sources of the calculation uncertainty are parameters taken from the MSIS model and also the collision cross-section estimation in the ion-neutral collisional frequency calculation.

Due to vertical lifting and continued solar production, the F_2 layer peak density is largely increased, which leads to enhanced field-aligned diffusion downward of the peak density. Further analysis of the four terms in the ambipolar diffusion equation confirmed that the first term within the parentheses is the dominant term at the altitude of the flow/flux peak. The nominal electron temperature increases with altitude at the PFISR latitude, while it decreases within the plume region in some events. This reduces the downward diffusion due to plasma temperature gradient. However, this effect is quite small compared with the density gradient change within the plumes. The contributions due to the other two terms in the diffusion equation are minor within the plumes.

Another factor that can affect the field-aligned flow speed is the thermospheric wind. The thermospheric wind can be estimated using $U_s = \frac{(V_{ap} - V_d)}{\cos I}$. Therefore, the thermospheric wind speeds that would be able to account for the difference between the measured field-aligned flow speed and the calculated ambipolar diffusion are
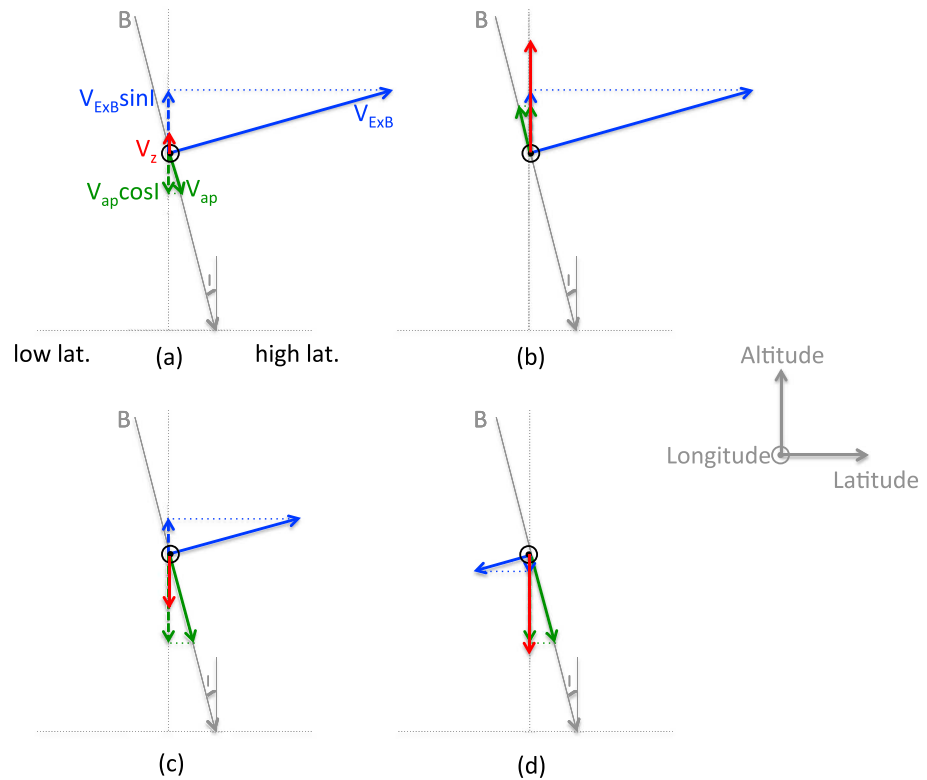
Figure 10. Four different geometries associated with induced plasma drifts in the meridional plane. V_{ap} and $V_{E\times B}$ represent antiparallel flow and $\mathbf{E}\times\mathbf{B}$ drift component in the meridional plane measured by PFISR.

$240\,\mathrm{m\,s}^{-1}$ and $577\,\mathrm{m\,s}^{-1}$. The nominal dayside thermospheric wind at the latitude of PFISR is poleward and $<200\,\mathrm{m\,s}^{-1}$ at 276 km [*Richards et al.*, 2009]. During geomagnetic storm times, the thermospheric wind pattern changes dramatically compared with quiet time [e.g., *Richmond and Matsushita*, 1975; *Richmond et al.*, 2003; *Lu et al.*, 2012; *Wang et al.*, 2008]. *Wang et al.* [2008] used the Coupled Magnetosphere-Ionosphere-Thermosphere model to study the horizontal wind variations during quiet and storm times. They found that during the storm event studied, the poleward thermospheric wind at 12 LT and 62.5° geographic latitude can increase substantially to >300 m/s around 300 km and >600 m/s around 500 km in the upper thermosphere. Further momentum acceleration analysis conducted by them shows that ion drag and pressure gradient dominate below and above 300 km, respectively. Preliminary GITM simulation results (not shown) of the November 2012 storm (storm B) also show largely enhanced poleward thermospheric wind to $>\sim300$ m/s at PFISR latitudes at 361 km in the noon to early afternoon sector during the time when the downward flux was observed by PFISR. The above simulation results suggest that the poleward thermospheric wind can increase during storm time to a magnitude that can account for the discrepancy between the calculated diffusion speed and the measured field-aligned flow speed. Statistical wind patterns from the CHAMP satellite within 131 days centered at June solstice for elevated geomagnetic activity times ($Kp=4-$) indeed show poleward thermospheric wind on the order of 200–300 m/s in the early afternoon sector [*Lühr et al.*, 2007].

At high latitudes, enhanced thermospheric winds are due to increased ion drag and Joule heating [*Richmond and Thayer*, 2000]. In Figure 9, the magnitudes of the $\mathbf{E}\times\mathbf{B}$ drift at 66° and 67° MLATs, and ion temperature averaged between 150 and 600 km from the field-aligned beam, i.e., beam 2 and another representative beam at higher latitude are shown for the September 2012 (storm C) and August 2010 (storm F) storms. Clearly, in the periods when downward flows were observed in Figure 6, there is enhanced convection flow speed to ~2000 m s^{-1} and enhanced ion temperature to >2500 K. Therefore, thermospheric wind speed is also expected to increase during these periods. Based on the convection flows measured by PFISR in Figure 3 and the GPS TEC/SuperDARN movies, these large convection flows are likely the western surge of the SAPS flow channels. *Wang et al.* [2012] included an empirical SAPS model in the TIEGCM model and studied the

SAPS effects on the thermosphere wind pattern. Their simulation results show a neutral temperature increase on the order of 50 K at ~300 km altitude near the western surge of the SAPS in their Figures 3a, 4e, and 4f.

4.3. Synthesized SED Plume Electrodynamic Features

Figure 10 shows four different geometries associated with induced plasma drifts in the meridional plane. The coordinates are shown to the right of the figure. The tilted grey line in each case is the magnetic field line, and I is the magnetic dip angle. The lengths of the vectors in each case are drawn aiming to present a clear illustration and are not suitable for cross comparison among different cases. In case (a), a strong eastward electric field exists, resulting in a strong northward $\mathbf{E} \times \mathbf{B}$ drift that is tilted slightly in the vertical direction. In addition, a small flow directed down the field line is imposed, caused by a combination of vertical forces (gravity and pressure gradient) and/or neutral winds. This antiparallel flow has a large component in the vertical direction. When this component is added to the vertical component of the $\mathbf{E} \times \mathbf{B}$ drift, the net flow is quite small, but slightly upward. In case (b), the field-aligned flow is up the field line, so the net result is a large upward flow. For case (c), the $\mathbf{E} \times \mathbf{B}$ drift is reduced and the downward field-aligned flow is increased, resulting in a net downward flow. In the last case (d), the $\mathbf{E} \times \mathbf{B}$ drift changes to have a small southward component, which will further increase the downward flow projected from the field-aligned component. This case is rare so that it is only occasionally observed near the equatorward boundary of the PFISR fov. We further mark corresponding cases for each event in Figure 3 in the third row of PFISR observation and also listed them in Table 1.

Overall, all the situations have been observed by PFISR within the SED plumes, suggesting the highly dynamic nature of the plumes. Figures 10a and 10b describe the situations of net positive vertical drifts, which are responsible for the plume density enhancement and in general the projection of the $\mathbf{E} \times \mathbf{B}$ drift dominates. These $\mathbf{E} \times \mathbf{B}$ drifts can be due to penetration electric field or they can be auroral and subauroral (SAPS) convection flows. Oppositely, Figures 10c and 10d describe the situation of net negative vertical drift, which are observed during the plume decay phase. Large downward field-aligned flow can be due to significantly modified pressure gradient and thus enhanced diffusion and also increased poleward thermospheric wind.

5. Summary and Conclusions

Storm-enhanced density (SED) plumes are prominent ionospheric electron density increases at the dayside middle and high latitudes. We study the generation and decay of electron densities within the plumes after the horizontal transport providing the initial seed population from the SED base region at lower latitudes. In order to study the generation mechanism of the enhanced density, three-dimensional plasma velocity measurements are required, which is not often available. In addition, the origin of the convection electric fields associated with the plumes and where they map to in the magnetosphere are still a much debated topic. Furthermore, the decay of the enhanced plume density has not been systematically studied before. In this study, SED plumes during six geomagnetic storms and associated key ionospheric parameters, including vertical ion flow, field-aligned ion flow and flux, plasma temperature, and field-aligned currents, have been studied using multiple instruments and their implications on the generation and decay of the SED plumes have been discussed. Results of this study are summarized below:

1. The peak TEC increase of the plumes observed at PFISR is ~1.4–5.5 times higher than the quiet time value.
2. Within the plumes, enhanced upward vertical ion flows with magnitude varying from a couple of tens $\mathrm{m\,s^{-1}}$ to over a hundred $\mathrm{m\,s^{-1}}$ are responsible for lifting the plasma to higher altitude in the sunlit region and thus resulting in density increase. The contributions from the $\mathbf{E} \times \mathbf{B}$ drift and from the antiparallel flow to the upward vertical ion flow are further analyzed, and it is almost completely due to the $\mathbf{E} \times \mathbf{B}$ drift projection in the vertical direction. This provides direct evidence for the imbalanced local production and loss mechanism, i.e., vertical plasma lifting, working within the plumes. In addition, upward vertical flows near the poleward part of the plumes are more persistent, while those near the equatorward are more patchy.
3. The northwestward $\mathbf{E} \times \mathbf{B}$ flows associated with the plumes range from a couple of hundred $\mathrm{m\,s^{-1}}$ to $>$ 1 $\mathrm{km\,s^{-1}}$, and are collocated with either upward or downward FACs but usually equatorward of the peak of the Region 1 upward FACs. This suggests the origin of these convection flows within the plumes; that is, they can be either subauroral or auroral flows.
4. There exists a steep electron temperature gradient within and surrounding the plumes. The electron temperature reached a minimum at the plume center and is inversely proportional to the density. Comparing the surrounding region and the plumes, the electron to ion temperature ratio reduces from ~2 to ~1.

5. In addition, during the decay phase of the plumes, large downward ion flows, as large as ~200 m s^{-1}, and fluxes, as large as 10^{14} m^{-2} s^{-1}, are often observed within the plumes. Enhanced ambipolar diffusion due to elevated pressure gradient is able to explain two out of the four large downward flow/flux cases but is not sufficient for the other two cases with stronger flows. For the latter two cases, enhanced poleward thermospheric wind is suggested to be another mechanism for pushing the plasma downward. These downward flows should be an important mechanism for the decay of the SED plumes. Direct thermospheric wind measurement in the future in this area would be ideal to further test the relative importance of these two mechanisms to the total field-aligned ion flows.

6. Within the plumes, four different geometries of induced plasma drifts have been inferred from PFISR observations, indicating the highly dynamic nature of the plumes.

References

Anderson, B. J., K. Takahashi, and B. A. Toth (2000), Sensing global Birkeland currents with Iridium® engineering magnetometer data, *Geophys. Res. Lett.*, *27*, 4045–4048, doi:10.1029/2000GL000094.

Anderson, B. J., K. Takahashi, T. Kamei, C. L. Waters, and B. A. Toth (2002), Birkeland current system key parameters derived from Iridium® observations: Method and initial validation results, *J. Geophys. Res.*, *107*(A6), 1079, doi:10.1029/2001JA000080.

Anderson, P. C., R. A. Heelis, and W. B. Hanson (1991), The ionospheric signatures of rapid subauroral ion drifts, *J. Geophys. Res.*, *96*, 5785–5792, doi:10.1029/90JA02651.

Aponte, N., M. J. Nicolls, S. A. Gonzalez, M. P. Sulzer, M. C. Kelley, E. Robles, and C. A. Tepley (2005), Instantaneous electric field measurements and derived neutral winds at Arecibo, *Geophys. Res. Lett.*, *32*, L12107, doi:10.1029/2005GL022609.

Borovsky, J. E., M. Hesse, J. Birn, and M. M. Kuznetsova (2008), What determines the reconnection rate at the dayside magnetosphere?, *J. Geophys. Res.*, *113*, A07210, doi:10.1029/2007JA012645.

Buonsanto, M. J., and O. G. Witasse (1999), An updated climatology of thermospheric neutral winds and *F* region ion drifts above Millstone Hill, *J. Geophys. Res.*, *104*, doi:10.1029/1999JA900345.

Chisham, G., et al. (2007), A decade of the Super Dual Auroral Radar Network (SuperDARN): Scientific achievements, new techniques and future directions, *Surv. Geophys.*, *28*, 33–109, doi:10.1007/s10712-007-9017-8.

Coster, A., and S. Skone (2009), Monitoring storm-enhanced density using IGS reference station data, *J. Geodesy*, *83*(3–4), 345–351.

David, M., J. J. Sojka, R. W. Schunk, M. W. Liemohn, and A. J. Coster (2011), Dayside midlatitude ionospheric response to storm time electric fields: A case study for 7 September 2002, *J. Geophys. Res.*, *116*, A12302, doi:10.1029/2011JA016988.

Deng, Y., and A. J. Ridley (2006), Role of vertical ion convection in the high-latitude ionospheric plasma distribution, *J. Geophys. Res.*, *111*, A09314, doi:10.1029/2006JA011637.

Doherty, P., A. J. Coster, and W. Murtagh (2004), Space weather effects of October–November 2003, *GPS Solutions*, *8*, 267–271.

Foster, J., W. Rideout, B. Sandel, W. Forrester, and F. Rich (2007), On the relationship of SAPS to storm-enhanced density, *J. Atmos. Terr. Phys.*, *69*, 303–313, doi:10.1016/j.jastp.2006.07.021.

Foster, J. C. (1993), Storm time plasma transport at middle and high latitudes, *J. Geophys. Res.*, *98*(A2), 1675–1689, doi:10.1029/92JA02032.

Foster, J. C., and W. J. Burke (2002), SAPS: A new characterization for sub-auroral electric fields, *Eos. Trans. AGU*, *83*, 393, doi:10.1029/2002EO000289.

Foster, J. C., and J. R. Doupnik (1984), Plasma convection in the vicinity of the dayside cleft, *J. Geophys. Res.*, *89*(A10), 9107–9113, doi:10.1029/JA089iA10p09107.

Foster, J. C., and W. Rideout (2005), Midlatitude TEC enhancements during the October 2003 superstorm, *Geophys. Res. Lett.*, *32*, L12S04, doi:10.1029/2004GL021719.

Foster, J. C., and H. B. Vo (2002), Average characteristics and activity dependence of the subauroral polarization stream, *J. Geophys. Res.*, *107*(A12), 1475, doi:10.1029/2002JA009409.

Foster, J. C., P. J. Erickson, A. J. Coster, J. Goldstein, and F. J. Rich (2002), Ionospheric signatures of plasmaspheric tails, *Geophys. Res. Lett.*, *29*(13), doi:10.1029/2002GL015067.

Foster, J. C., et al. (2005), Multiradar observations of the polar tongue of ionization, *J. Geophys. Res.*, *110*, A09S31, doi:10.1029/2004JA010928.

Foster, J. C., P. J. Erickson, A. J. Coster, S. Thaller, J. Tao, J. R. Wygant, and J. W. Bonnell (2014), Storm time observations of plasmasphere erosion flux in the magnetosphere and ionosphere, *Geophys. Res. Lett.*, *41*, 762–768, doi:10.1002/2013GL059124.

Fuller-Rowell, T. (2011), Storm-time response of the thermosphere–ionosphere system, in *Aeronomy of the Earth's Atmosphere and Ionosphere*, *IAGA Spec. Sopron Book Ser.*, vol. 2, edited by M. A. Abdu and D. Pancheva, pp. 419–434, Springer, Dordrecht, Netherlands, doi:10.1007/978-94-007-0326-1_32.

Galperin, Y., V. Ponomarev, and A. Zosimova (1974), Plasma convection in the polar ionosphere, *Ann. Geophys.*, *30*, 1.

Greenwald, R. A., et al. (1995), DARN/SuperDARN: A global view of the dynamics of high-latitude convection, *Space Sci. Rev.*, *71*, 761–796, doi:10.1007/BF00751350.

Heelis, R. A., J. J. Sojka, M. David, and R. W. Schunk (2009), Storm time density enhancements in the middle-latitude dayside ionosphere, *J. Geophys. Res.*, *114*, A03315, doi:10.1029/2008JA013690.

Heinselman, C. J., and M. J. Nicolls (2008), A Bayesian approach to electric field and *E*-region neutral wind estimation with the Poker Flat Advanced Modular Incoherent Scatter Radar, *Radio Sci.*, *43*, RS5013, doi:10.1029/2007RS003805.

Huang, C.-S., J. C. Foster, L. P. Goncharenko, P. J. Erickson, W. Rideout, and A. J. Coster (2005), A strong positive phase of ionospheric storms observed by the Millstone Hill incoherent scatter radar and global GPS network, *J. Geophys. Res.*, *110*, A06303, doi:10.1029/2004JA010865.

Ledvina, B. M., J. J. Makela, and P. M. Kintner (2002), First observations of intense GPS L1 amplitude scintillations at mid-latitude, *Geophys. Res. Lett.*, *29*(14), 1659, doi:10.1029/2002GL014770.

Loranc, M., and J.-P. St.-Maurice (1994), A time-dependent gyro-kinetic model of thermal ion upflows in the high-latitude *F* region, *J. Geophys. Res.*, *99*(A9), 17,429–17,451, doi:10.1029/93JA01852.

Loranc, M., W. B. Hanson, R. A. Heelis, and J.-P. St.-Maurice (1991), A morphological study of vertical ionospheric flows in the high-latitude *F* region, *J. Geophys. Res.*, *96*(A3), 3627–3646, doi:10.1029/90JA02242.

Lu, G., L. Goncharenko, M. J. Nicolls, A. Maute, A. Coster, and L. J. Paxton (2012), Ionospheric and thermospheric variations associated with prompt penetration electric fields, *J. Geophys. Res.*, *117*, A08312, doi:10.1029/2012JA017769.

Lu, G., J. D. Huba, and C. Valladares (2013), Modeling ionospheric super-fountain effect based on the coupled TIMEGCM-SAMI3, *J. Geophys. Res. Space Physics*, *118*, 2527–2535, doi:10.1002/jgra.50256.

Lühr, H., S. Rentz, P. Ritter, H. Liu, and K. Häusler (2007), Average thermospheric wind patterns over the polar regions, as observed by CHAMP, *Ann. Geophys.*, *25*, 1093–1101, doi:10.5194/angeo-25-1093-2007.

Mannucci, A. J., B. D. Wilson, D. N. Yuan, C. H. Ho, U. J. Lindqwister, and T. F. Runge (1998), A global mapping technique for GPS-derived ionospheric total electron content measurements, *Radio Sci.*, *33*(3), 565–582, doi:10.1029/97RS02707.

Mannucci, A. J., B. T. Tsurutani, B. A. Iijima, A. Komjathy, A. Saito, W. D. Gonzalez, F. L. Guarnieri, J. U. Kozyra, and R. Skoug (2005), Dayside global ionospheric response to the major interplanetary events of October 29–30, 2003 "Halloween Storms," *Geophys. Res. Lett.*, *32*, L12S02, doi:10.1029/2004GL021467.

Moen, J., K. Oksavik, L. Alfonsi, Y. Daabakk, V. Romano, and L. Spogli (2013), Space weather challenges of the polar cap ionosphere, *J. Space Weather Space Clim.*, *3*, A02.

Ogawa, Y., S. C. Buchert, R. Fujii, S. Nozawa, and A. P. van Eyken (2009), Characteristics of ion upflow and downflow observed with the European Incoherent Scatter Svalbard radar, *J. Geophys. Res.*, *114*, A05305, doi:10.1029/2008JA013817.

Picone, J. M., A. E. Hedin, D. P. Drob, and A. C. Aikin (2002), NRLMSISE-00 empirical model of the atmosphere: Statistical comparisons and scientific issues, *J. Geophys. Res.*, *107*(A12), 1468, doi:10.1029/2002JA009430.

Pintér, B., S. D. Thom, R. Balthazor, H. Vo, and G. J. Bailey (2006), Modeling subauroral polarization streams equatorward of the plasmapause footprints, *J. Geophys. Res.*, *111*, A10306, doi:10.1029/2005JA011457.

Richards, P. G., M. J. Nicolls, C. J. Heinselman, J. J. Sojka, J. M. Holt, and R. R. Meier (2009), Measured and modeled ionospheric densities, temperatures, and winds during the international polar year, *J. Geophys. Res.*, *114*, A12317, doi:10.1029/2009JA014625.

Richmond, A. D., and S. Matsushita (1975), Thermospheric response to a magnetic substorm, *J. Geophys. Res.*, *80*(19), 2839–2850, doi:10.1029/JA080i019p02839.

Richmond, A. D., and J. P. Thayer (2000), Ionospheric electrodynamics: A tutorial, in *Magnetospheric Current Systems*, *Geophys. Monogr. Ser.*, vol. 118, edited by S.-I. Ohtani et al., pp. 131–146, AGU, Washington, D. C., doi:10.1029/GM118p0131.

Richmond, A. D., C. Lathuillère, and S. Vennerstroem (2003), Winds in the high-latitude lower thermosphere: Dependence on the interplanetary magnetic field, *J. Geophys. Res.*, *108*(A2), 1066, doi:10.1029/2002JA009493.

Rideout, W., and A. Coster (2006), Automated GPS processing for global total electron content data, *GPS Solut.*, *10*(3), 219–228, doi:10.1007/s10291-006-0029-5.

Ruohoniemi, J. M., and K. B. Baker (1998), Large-scale imaging of high-latitude convection with Super Dual Auroral Radar Network HF radar observations, *J. Geophys. Res.*, *103*(A9), 20,797–20,811, doi:10.1029/98JA01288.

Saito, A., S. Fukao, and S. Miyazaki (1998), High resolution mapping of TEC perturbations with the GSI GPS network over Japan, *Geophys. Res. Lett.*, *25*(16), 3079–3082, doi:10.1029/98GL52361.

Sellek, R., G. J. Bailey, R. J. Moffett, R. A. Heelis, and P. C. Anderson (1991), Effects of large zonal plasma drifts on the subauroral ionosphere, *J. Atmos. Terr. Phys.*, *53*, 557–565, doi:10.1016/0021-9169(91)90083-J.

Shepherd, S. G., and J. M. Ruohoniemi (2000), Electrostatic potential patterns in the high-latitude ionosphere constrained by SuperDARN measurements, *J. Geophys. Res.*, *105*(A10), 23,005–23,014, doi:10.1029/2000JA000171.

Skone, S., R. Yousuf, and A. Coster (2004), Performance evaluation of the wide area augmentation system for ionospheric storm events, *Journal of Global Positioning Systems*, *3*(1–2), 251–258.

Sojka, J. J., M. J. Nicolls, C. J. Heinselman, and J. D. Kelly (2009), The PFISR IPY observations of ionospheric climate and weather, *J. Atmos. Sol. Terr. Phys.*, *71*, 771–785, doi:10.1016/j.jastp.2009.01.001.

Southwood, D. J., and R. A. Wolf (1978), An assessment of the role of precipitation in magnetospheric convection, *J. Geophys. Res.*, *83*(A11), 5227–5232, doi:10.1029/JA083iA11p05227.

Spiro, R. W., R. A. Heelis, and W. B. Hanson (1979), Rapid subauroral ion drifts observed by Atmospheric Explorer C, *Geophys. Res. Lett.*, *6*, 657–660, doi:10.1029/GL006i008p00657.

Sun, Y.-Y., T. Matsuo, E. A. Araujo-Pradere, and J.-Y. Liu (2013), Ground-based GPS observation of SED-associated irregularities over CONUS, *J. Geophys. Res. Space Physics*, *118*, 2478–2489, doi:10.1029/2012JA018103.

Thomas, E. G., J. B. H. Baker, J. M. Ruohoniemi, L. B. N. Clausen, A. J. Coster, J. C. Foster, and P. J. Erickson (2013), Direct observations of the role of convection electric field in the formation of a polar tongue of ionization from storm enhanced density, *J. Geophys. Res. Space Physics*, *118*, 1180–1189, doi:10.1002/jgra.50116.

Tsurutani, B. T., et al. (2004), Global dayside ionospheric uplift and enhancement associated with interplanetary electric fields, *J. Geophys. Res.*, *109*, A08302, doi:10.1029/2003JA010342.

Tsurutani, B. T., A. J. Mannuccci, O. P. Verkhoglyadova, and G. S. Lakhina (2013), Comment on "Storming the Bastille: The effect of electric fields on the ionospheric *F*-layer" by Rishbeth et al. (2010), *Ann. Geophys.*, *31*, 145–150, doi:10.5194/angeo-31-145-2013.

Walsh, B. M., J. C. Foster, P. J. Erickson, and D. G. Sibeck (2014), Simultaneous ground- and space-based observations of the plasmaspheric plume and reconnection, *Science*, *343*(6175), 1122–1125.

Wang, W., A. G. Burns, M. Wiltberger, S. C. Solomon, and T. L. Killeen (2008), Altitude variations of the horizontal thermospheric winds during geomagnetic storms, *J. Geophys. Res.*, *113*, A02301, doi:10.1029/2007JA012374.

Wang, W., J. Lei, A. G. Burns, S. C. Solomon, M. Wiltberger, J. Xu, Y. Zhang, L. Paxton, and A. Coster (2010), Ionospheric response to the initial phase of geomagnetic storms: Common features, *J. Geophys. Res.*, *115*, A07321, doi:10.1029/2009JA014461.

Wang, W., E. R. Talaat, A. G. Burns, B. Emery, S. Hsieh, J. Lei, and J. Xu (2012), Thermosphere and ionosphere response to subauroral polarization streams (SAPS): Model simulations, *J. Geophys. Res.*, *117*, A07301, doi:10.1029/2012JA017656.

Whalen, J. A. (1989), The daytime *F* layer trough and its relation to ionospheric-magnetospheric convection, *J. Geophys. Res.*, *94*(A12), 17,169–17,184, doi:10.1029/JA094iA12p17169.

Yeh, H.-C., J. C. Foster, F. J. Rich, and W. Swider (1991), Storm time electric field penetration observed at mid-latitude, *J. Geophys. Res.*, *96*(A4), 5707–5721, doi:10.1029/90JA02751.

Zou, S., A. J. Ridley, M. B. Moldwin, M. J. Nicolls, A. J. Coster, E. G. Thomas, and J. M. Ruohoniemi (2013), Multi-instrument observations of SED during 24–25 October 2011 storm: Implications for SED formation processes, *J. Geophys. Res. Space Physics*, *118*, 7798–7809, doi:10.1002/2013JA018860.